Study of Multicomponent Diffusion in Entangled *cis*-Polyisoprene Melts by Normal-Mode Microdielectrometry

Jeffrey S. Fodor and Davide A. Hill*

Department of Chemical Engineering, University of Notre Dame du Lac, Notre Dame, Indiana 46556

Received July 13, 1994; Revised Manuscript Received November 23, 1994[⊗]

ABSTRACT: We combine microdielectrometry (MD) sensors with polymers showing dielectric normal-mode relaxation (type A polymers) to study multicomponent diffusion in melts of entangled, linear, flexible chains. The term "normal-mode microdielectrometry" (NMMD) reflects this particular combination of ingredients. We consider *cis*-polyisoprene (*cis*-PI), a well-characterized type A polymer. Using reptation theory and a linear mixing rule, normal-mode dielectric loss spectra of polydisperse *cis*-PI samples can be inverted to yield the entire molecular weight distribution (MWD). MD sensors enable probing the dielectric response of the material residing in the immediate vicinity (O(10 μm)) of a solid surface. Therefore, the combination of type A polymers and MD sensors allows us to follow the evolution of the MWD of the material in the immediate proximity of a solid surface. We study the diffusive dissolution of a thin layer of a polydisperse, high-MW *cis*-PI melt, deposited at the sensor surface, into a polydisperse, semiinfinite medium of smaller chains. The data are first analyzed using a Fickian diffusion model with a molecular weight dependent effective diffusivity. The results are consistent with swelling of the high-MW melt caused by diffusive penetration of smaller chains. We also propose an extension of the Kramer−Sillescu theory of diffusion to polydisperse systems and contrast the results to the kinetic-theory equations of Bird et al. An analytical solution for the evolving near-surface MWD is obtained for a simplistic version of the Bird et al. model. Although showing qualitatively correct trends, the model is unable to quantitatively describe the experimental data.

Introduction

Polymer−polymer interdiffusion is important to a variety of industrial applications (e.g., polymerization,[1] dissolution, homogenization, adhesion,[2] welding,[3] etc.). Additionally, the mechanisms controlling macromolecular motion within melts and solutions are known to be relevant to other important observables (such as rheological properties, for instance).[4] The motivation for understanding such processes is thus justified pragmatically as well as fundamentally.

Several investigations have been conducted to elucidate the mechanism of chain diffusion in dense systems. Theoretical and experimental progress through 1989 has been reviewed by Tirrell and Kausch.[3] Analysis of diffusion in concentrated systems is complicated by the large size and connectivity of the chains and by mass balance constraints. Above entanglement, substantial difficulties arise in connection with the effects of topological constraints on chain mobility. In self-diffusion or tracer diffusion studies on entangled systems, the reptation model proposed by de Gennes[5] has been fairly successful in describing the observed phenomenology. For interdiffusion of two homopolymers of different chain lengths present in comparable amounts, the mobility of the species is dependent not only on their individual sizes but also on mutual interactions. This coupling endows the binary diffusion coefficient with a strong dependence on composition. Kramer et al.[6] showed theoretically, and verified experimentally, that the larger of two homopolymers placed in contact with each other will swell at a rate controlled by the mobility of the smaller chains. Similar experiments performed by other authors[7,8] showed comparable effects. Kramer et al.[6] followed by Sillescu[9,10] developed a theoretical treatment linking the binary diffusivity to the self-diffusion coefficients of the species in the couple. Kramer's result conflicted with an earlier one given by Brochard et al.,[11] where interdiffusion was predicted to be controlled by the mobility of the slow species. Further experiments,[12,13] theoretical work by Sillescu,[9] and a revised treatment by Brochard-Wyart[14] seem to have now resolved this controversy in favor of Kramer's analysis. Although these theories were tailored to describe binary couples, for which experimental evidence exists, they can be easily extended to multicomponent systems.

A theory for multicomponent diffusion in polymer melts has also been proposed by Bird et al.[15] based on kinetic theory formalism. The model has the advantage of predicting mass transfer as well as rheological properties. Bird et al.'s results differ from those we obtain following the Kramer−Sillescu formalism.

Experimental techniques for monitoring diffusion in polymer melts have included small-angle neutron scattering (SANS),[16] forward recoil spectroscopy (FRES),[17] pulsed field gradient NMR (PFG-NMR),[18] infrared attenuated total reflectance (ATR),[19] infrared microdensitometry (IRM),[12] secondary ion mass spectroscopy (SIMS),[20] and forced Raleigh scattering (FRS)[21] among others.[3,22] Most of these methods (PFG-NMR and marker experiments excluded) require introduction of some type of chemical distinction (tagging) on the species to be followed. The use of chemically modified chains can introduce two possible limitations, however. First, care must be taken to ensure that the change does not affect the thermodynamic compatibility of the guest molecules and the host matrix. This is especially crucial at high molecular weights, where entropic driving forces favoring mixing are weak. Second, each experiment is limited to monitoring the concentration of only the tagged species. Although PFG-NMR does not require tagging, it does not offer capability of discriminating between chains of different sizes. These limitations are of little consequence for self-diffusion or mutual diffu-

* Author to whom correspondence should be addressed.

[⊗] Abstract published in *Advance ACS Abstracts,* January 15, 1995.

0024-9297/95/2228-1271$09.00/0

sion studies with narrowly disperse couples and when thermodynamic effects can either be minimized or tested. On the other hand, studies on binary systems may not often reflect typical conditions of technological interest, where polydispersity can be a factor. Experiments on polydisperse systems are expected to put to a more stringent test available theories of diffusion. Use of the above methods would require a vast number of experiments to be performed, each starting from a different "chemical" initial condition. This is clearly an impractical and costly proposition.

In this paper we introduce a new experimental method that utilizes polymers endowed with a natural chemical distinction, namely, a global, permanent dipole moment parallel to the end-to-end vector of the chain. Therefore, the method does not require tagging. Such polymers were classified by Stockmayer as of the type A[23] and include *cis*-polyisoprene, poly(propylene oxide), poly(benzyl glutamate), and poly(*n*-alkyl isocyanates) (and possibly many others of which we are presently unaware). (Of the above polymers, the former two are flexible coillike, while the remaining ones usually assume a rodlike conformation in solution.) In the present work we shall focus on *cis*-polyisoprene (*cis*-PI), for its well-characterized dielectric properties.[24-31] The permanent dipole parallel to the end-to-end vector of the chain endows *cis*-PI with a normal-mode dielectric loss spectrum that is sensitive to main-chain (normal-mode) relaxation processes. In entangled melts, where relaxation occurs by reptation, the dielectric relaxation time of each species is strongly dependent on the molecular weight of that species. The dielectric loss spectrum of a polydisperse melt of flexible type A polymers is then highly sensitive to composition. Hence, with an appropriate model for single-chain dynamics (the single-chain autocorrelation function) and a descriptor of multicomponent interactions (the mixing rule) the entire molecular weight distribution (MWD) of a type A melt can be determined from inversion of its dielectric loss spectrum.[32]

The ability to monitor melt composition is only a necessary condition for diffusion studies. The use of type A polymers must then be coupled to a tool capable of detecting the evolution of composition in one or more regions of the experimental system. We have recently demonstrated that microdielectrometry (MD) sensors offer this opportunity,[30] allowing one to probe dielectrically an extremely localized region near the sensor surface. A MD sensor (described in more detail later on) is a capacitor formed by photolythographic deposition of interdigitated-comb electrodes on a nonconducting substrate. The penetration depth of the electric field above the sensor surface (which defines the dielectric control volume) scales with the spacing between the lines and can be controlled by design. In the present study, sensors with electrode spacings of 50 μm were used, leading to a field penetration depth of about 13 μm. Therefore, the combination of type A polymers and microdielectrometry sensors permits measurement of the molecular weight distribution of a melt (or solution) in the neighborhood of a solid surface. The term "normal-mode microdielectrometry" (NMMD) reflects this particular combination of ingredients.

This paper is structured as follows. First, prediction and inversion of normal-mode (NM) dielectric loss spectra are briefly reviewed. A discussion of sensor structure and properties follows. We then propose an extension of the Kramer–Sillescu theory to multicomponent systems and contrast the results to those of the Bird et al. theory. Conservation equations and constitutive relations for the fluxes are first derived for systems with discrete molecular weight distribution and then extended to the case of a continuous mixture. Both the Kramer–Sillescu and Bird et al. theories lead to nonlinear equations, which require numerical solution. Such an effort is not attempted here. The experimental results are thus presented and analyzed to the lowest order of approximation using at first a simple Fickian diffusion model. As it turns out, an analytical solution for evolution of near-surface composition can be obtained in the continuum limit for a simplified version of the Bird et al. model. This treatment will be offered toward the end of the paper, and the results will be compared to experimental data.

Inversion of Dielectric Loss Spectra

cis-Polyisoprene is characterized by a permanent dipole moment parallel to the end-to-end vector of the chain.[23-31] This trait results in a normal-mode (NM) dielectric loss spectrum $\epsilon''(\omega)$ that is strongly dependent on polymer molecular weight and composition. Rouse and glassy loss peaks also contribute to the spectrum, but they can be decoupled from the NM process by suitable procedures.[32] We shall focus on the normal-mode relaxation, for its proven ability to yield information on melt composition.[31,32]

We have recently shown[31] that a linear mixing rule[33] and the autocorrelation function of reptation[4] provide accurate predictions for NM dielectric loss spectra of moderately polydisperse *cis*-PI melts above entanglement. (Linear mixing implies composition-independent dielectric relaxation times. Adachi et al.[34] reported a failure of this hypothesis in highly polydisperse blends. In the present study we were thus cautious to use samples for which linear mixing has been unquestionably established to hold.[31]) The relevant equations can be summarized as follows (see refs 31 and 32 for details):

$$\epsilon''(\omega) = (\epsilon_0 - \epsilon_\infty) \sum_{i=1}^{L} \phi_i F(\omega\tau_i) \tag{1}$$

$$F(\omega\tau_i) = \frac{8}{\pi^2} \sum_{\substack{p=1 \\ p=\text{odd}}}^{\infty} \frac{\omega\tau_i}{p^4 + (\omega\tau_i)^2} \tag{2}$$

$$\tau_i = \tau_0 (M_i/M_0)^m \tag{3}$$

where ω is the frequency, ϕ_i and τ_i are the mass fraction and relaxation time of species with molecular weight M_i, respectively, τ_0 and M_0 are the reference relaxation time and molecular weight, respectively, and ϵ_0 and ϵ_∞ are the limiting permittivities at vanishing and infinite frequency, respectively. The dielectric strength $(\epsilon_0 - \epsilon_\infty)$ is temperature dependent but insensitive to the MW.[27,31,32] Although reptation theory predicts $m = 3$, we have found that correct prediction of both the shape and frequency position of loss spectra of *cis*-PI melts requires the use of $m = 3.70$.[24-28,31,32,35] In eq 1 the MWD is specified in the form of $L - 1$ mass fractions.

Inversion of experimental loss spectra to determine the MWD is an ill-posed problem which requires the use of regularization techniques. In a recent paper[32] loss spectra of *cis*-PI melts were successfully inverted by either Tikhonov regularization[36,37] or a regula–falsi algorithm (RFA) proposed by Imanishi and co-workers.[38]

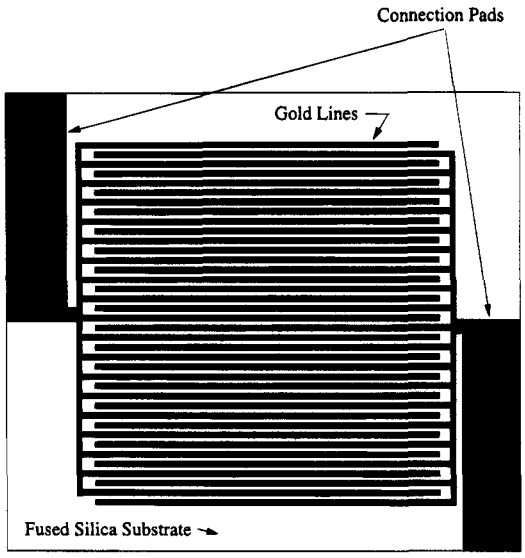

Figure 1. Schematic of sensor layout. The dark lines are the photolythographically-deposited electrodes, and the two rectangular areas on the left and right of the sensing array are connection pads. For clarity, the total number of lines on the sensor has been reduced.

Details about these methods are given in ref 32 and will not be discussed here. In the present work primarily the RFA method was used, although, occasionally, some of the inversions were also verified by Tikhonov regularization. The RFA inversions used self-consistent fits determined by method 2 as detailed in ref 32. In our previous work we found that, for the same samples used in the present study, RFA inversions were sufficiently accurate to capture the MWD measured by SEC within root-mean-square error of ±6% of the peak value. (This resolution depends on the magnitude of the noise and is essentially identical to that achievable by Tikhonov regularization.) Although the RFA method can certainly be refined, we believe that this resolution is adequate to warrant the present work. We recognize, however, that the accuracy of the inversions may be poor at very high and very low molecular weights, where the MWDs fall below about 10% of their peak value. (This uncertainty incorporates errors arising from imperfect extrapolation of the spectra in experimentally unaccessible regions.[32])

The Dielectric Sensor

A dielectric sensor (hereafter occasionally referred to as "the chip") is a capacitor formed by photolythographic deposition of interdigitated combs of conducting lines on a nonconducting substrate. Figure 1 schematically illustrates the topography of the device. The sensors used in this study were designed in our laboratory and manufactured by Thin Film Technology, Buellton, CA. Each chip consists of 160 gold lines, 2 μm thick, 25 μm wide, 7.5 mm long, and spaced 50 μm apart (axis-to-axis), patterned on a fused-silica substrate. For a sensing area of 0.60 cm^2, an overall capacitance of about 29 pF results in air (this value includes the substrate contribution).

The electric field distribution above the sensor surface can be calculated from standard electrostatic theory.[30,39,40] Two important features emerge from the analysis.[30,40] The electric field is two-dimensional and periodic, lying in a plane perpendicular to the lines. This makes it possible to detect dielectric anisotropy.[40] The field decays exponentially away from the surface over a length scale comparable to the line spacing. The dielectric control volume is then confined to a narrow region immediately above the sensor surface. The above features have allowed us to probe near-wall structure in flowing liquid crystals[40] and flow-induced fractionation in *cis*-PI melts.[30]

For a heterogeneous dielectric placed in a nonuniform electric field, the measured permittivity, $\langle\epsilon\rangle$, reflects the energy density average of the permittivity over the volume probed by the field, ν:[30,40,41]

$$\langle\epsilon\rangle = \int_\nu \epsilon(\vec{r})\,\Phi(\vec{r})\,d\vec{r}^3 \tag{4}$$

$$\Phi(\vec{r}) = E^2(\vec{r}^2)/\int_\nu E^2(\vec{r})\,d\vec{r}^3 \tag{5}$$

where $\Phi(\vec{r})$ is the energy-density distribution function and E is the electric field. For a periodic array of metal lines of width W, spaced by a distance $2W$ (axis-to-axis), the following one-dimensional approximation of $\Phi(\vec{r})$ is appropriate:

$$\Phi(x) = (\pi/L)(\cosh(\pi x/L))^{-2} \tag{6}$$

where x is the distance from the surface, and $L = 1.70W$.[40] For the sensors used in this study $W = 25$ [μm], giving $L = 42.5$ [μm], and a field penetration depth $(L/\pi) = 13.5$ [μm].

As indicated by eqs 4–6, the measured permittivity may generally incorporate information from near-surface and bulk material.[30,40] The experimental system, however, can be designed to selectively probe the near-surface material only. The present experiments were performed by depositing on the sensor a thin layer of a high molecular weight polymer and then overlaying to that a copious amount of a second melt of lower molar mass (to give an essentially semiinfinite medium). Mathematically, this geometry dictates two important features: (1) the characteristic length scale for diffusion is the original thickness of the high molecular weight layer, δ, and (2) the no-flux boundary condition at the solid surface ($x = 0$) forces the density profiles of all species to be even in x. Consequently, nearly flat profiles (hence ϵ'' from eqs 1 and 2) are obtained in the dielectric control volume, provided that a layer thickness much larger than the field penetration depth is chosen. In our experiments, δ ranged from 74 to 84 μm and $L/\pi = 13.5$ μm. In Appendix A we show that density inhomogeneity over the field penetration depth produces an error not exceeding $(L/\pi\delta)^2$, which, in our case, corresponds to about 3%.

Sensor calibration at a set frequency has been discussed in ref 40. In the present studies calibration over the entire experimental frequency range was required. For our sensors, the measured capacitance and the reciprocal of the product of resistance by the frequency are a linear combination of the real, ϵ', and imaginary, ϵ'', components of the complex dielectric permittivity of the sample and the substrate. The measured dielectric loss, ϵ''_m, can then be expressed as[40]

$$\epsilon''_m = k\epsilon''_{fs} + (1 - k)\epsilon''_s \tag{7}$$

where ϵ''_s and ϵ''_{fs} are the loss spectra of the sample and the fused silica substrate, respectively, and k is a constant (independent of tested material) quantifying the partitioning of the electric field in the substrate and the sample (for the sensors used here $k = 0.44$). The intrinsic response of the chip was first determined in

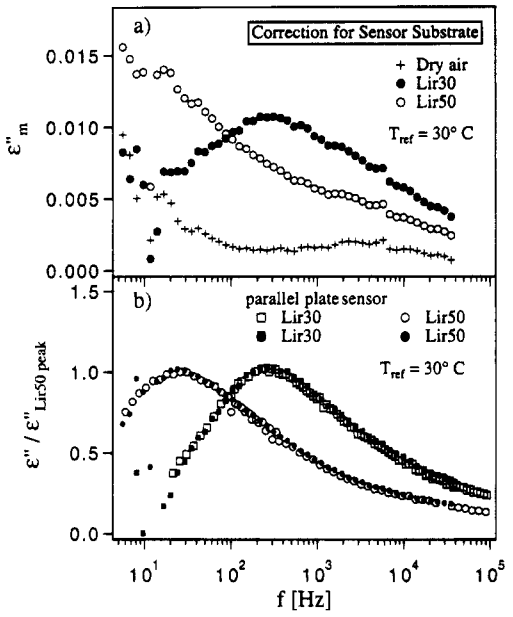

Figure 2. (a) Raw spectra, ϵ''_m as described in the text, acquired from the MD sensor for two *cis*-PI melts (Lir30 and Lir50) and dry air. (b) The spectra of part a corrected for sensor response and compared to parallel-plate measurements. The spectra have been normalized by the peak value for Lir50.

dry air, which has a negligible dielectric loss (as confirmed by parallel-plate measurements). The loss spectra of polymer samples were corrected by subtracting the dry-air spectrum and then renormalizing the data according to eq 7. Figure 2a displays the raw spectra for two *cis*-PI melts (Lir30 and Lir50 described later on) and dry air. The corrected spectra are compared to parallel-plate measurements in Figure 2b.

Theory

In this section we extend the Kramer–Sillescu theory to polydisperse mixtures and compare the results to those of the Bird et al. model. The equations are first derived for discrete mass fractions and then converted to describe a continuous distribution of molecular weights. Elastic effects on diffusion[42,43] will be ignored.

We consider the motion of chain i in a polydisperse melt of L interdiffusing species. The total force, $\mathbf{f}_i$, acting on the chain is

$$\mathbf{f}_i = -\xi_i(\mathbf{v}_i^{\,b} - \mathbf{v}^d) \tag{8}$$

where ξ_i is the friction coefficient of species i, $\mathbf{v}_i^{\,b}$ the center-of-mass diffusional velocity by Brownian motion, and $\mathbf{v}^d$ the velocity field created by the collective, diffusive motion of all species in the matrix. Physically, $\mathbf{v}^d$ would correspond to the net swelling rate of a high molecular weight polymer as caused by diffusive penetration of smaller chains.[6,9]

The Brownian velocity is obtained as:

$$\mathbf{v}_i^{\,b} = \mathbf{f}_i^{\,b}/\xi_i = -\nabla\mu_i/\xi_i \tag{9}$$

where $\mathbf{f}_i^{\,b}$ is the force caused by gradients in the species' chemical potential, μ_i. The mass flux $\mathbf{J}_i$ is given by

$$\mathbf{J}_i = \varrho\phi_i(\mathbf{v}_i^{\,b} + \mathbf{v}^d + \bar{\mathbf{v}}) = \varrho\phi_i(-\nabla\mu_i/\xi_i + \mathbf{v}^d + \bar{\mathbf{v}}) \tag{10}$$

where ϱ is the constant total density, $\bar{\mathbf{v}}$ the mass-average velocity ($\nabla\cdot\bar{\mathbf{v}} = 0$), and ϕ_i the mass (or volume) fraction of species i ($\sum_j\phi_j = 1$). Hereafter, summations are implicitly extended to all species (1 to L), unless noted otherwise. Incompressibility requires the sum of all mass fluxes referenced to a coordinate frame moving with the mass-average velocity to vanish:

$$\varrho\bar{\mathbf{v}} - \sum_j \mathbf{J}_j = 0 \tag{11}$$

giving

$$\mathbf{v}^d = \sum_j \phi_j\nabla\mu_j/\xi_j \tag{12}$$

and

$$\mathbf{J}_i = \varrho\phi_i(-\nabla\mu_i/\xi_i + \sum_j \phi_j\nabla\mu_j/\xi_j + \bar{\mathbf{v}}) \tag{13}$$

Henceforth, we will assume ($\bar{\mathbf{v}} = 0$), as relevant to our experiments.

Calculation of the chemical potential requires an expression for the free energy of mixing, F. We adopt a Flory–Huggins functionality:[44]

$$F = k_B T(\sum_j n_j \ln\phi_j + \sum_j\sum_k \chi_{jk} n_j\phi_k) \tag{14}$$

where k_B and T are Boltzmann's constant and temperature, respectively, n_j is the number of molecules of species j, and χ_{jk} is the interaction-function matrix ($\chi_{\alpha\beta} = \chi_{\beta\alpha}$, $\chi_{\alpha\alpha} = 0$). For melts of homopolymers above entanglement: $\chi_{jk} = 0\ \forall\ j, k \in (1, L)$. (Note that this assumption may be invalid if variations of melt density with composition occur and/or heterogeneities in chain microstructures exist. In *cis*-PI, mixing of species with significantly different cis/trans ratios could bring about thermodynamic compatibility problems. A detailed account of such an effect is difficult at the present stage, even experimentally. Here we assume $\chi_{jk} = 0$.) The chemical potential, μ_i, is then:

$$\mu_i - \mu_i^{\,0}(T, P) = (\partial F/\partial n_i)_{T,P,n_{j\neq i}} = k_B T\left(\ln\phi_i + 1 - N_i\sum_j \frac{\phi_j}{N_j}\right) \tag{15}$$

where N_i and $\mu_i^{\,0}(T, P)$ are the degree of polymerization and the pure-component chemical potential of species i, respectively.

The expression for the flux becomes

$$\mathbf{J}_i = -\varrho D_i(\nabla\phi_i - \phi_i N_i\nabla\langle 1/N\rangle) + \phi_i\sum_j \varrho D_j(\nabla\phi_j - \phi_j N_j\nabla\langle 1/N\rangle) \tag{16}$$

$$D_i = k_B T/\xi_i \tag{17}$$

$$\langle 1/N\rangle = \sum_k \phi_k/N_k \tag{18}$$

Unlike the binary case,[6,9] the $\mathbf{J}_i$ can no longer be expressed in terms of $\nabla\phi_i$ only, since $\langle 1/N\rangle$ is now a function of $L - 1$ independent mass fractions. Equation 16 clearly evidences the meaning of $\mathbf{v}^d$ in eq 12. For non-Brownian particles, such as the gold markers used by Kramer et al., $D_m \approx 0$, and the marker flux is governed by the net swelling rate of the matrix (eq 12).

The friction coefficients in eq 17, ξ_i, assume the form:

$$\xi_i = \xi_e(N_i/N_e)^m \tag{19}$$

where N_e and ξ_e are the degree of polymerization and friction coefficient at the entanglement molecular weight, respectively. For fully entangled, reptating chains ($N_i/N_e \gg 1$), $m = 2$, while for unentangled chains ($N_i/N_e \ll 1$), $m = 1$. Note that eq 19 is only valid asymptotically, for the entanglement transition is smooth and its location depends on composition. Sillescu[9] proposed that the D_i should coincide with the self-diffusion coefficients of the species. This assumption should hold as long as ξ_e is independent of melt composition, which may not be true if changes in free volume occur during diffusion (in which case ξ_e will be a function of $\langle 1/N\rangle$[45]). (Of course, we are not considering more severe limitations in the model. Constraint release and tube renewal[46,47] will alter eq 19, by shifting the entanglement threshold and reducing the exponent.)

The conservation equations for the species assume the standard form:

$$\varrho \frac{\partial \phi_i}{\partial t} = -\nabla \cdot \mathbf{J}_i; \quad i = 1 \text{ to } L-1 \tag{20}$$

where only $L - 1$ equations are independent, as dictated by $\sum_j \phi_j = 1$ and eq 11. Equations 16–20 reduce to the expressions of Kramer and Sillescu for the case of a binary mixture.

On the basis of kinetic theory formalism, Bird et al. derived the following expression for the flux (with $\bar{\mathbf{v}} = 0$):

$$\mathbf{J}_i = \varrho(-\mathrm{D}_i \nabla \phi_i + \phi_i \sum_j \mathrm{D}_j \nabla \phi_j) \tag{21}$$

They also proposed that D_i should approach the tracer diffusion coefficients as $\phi_i \to 0$. Consequently, in a highly polydisperse melt, the D_i should also be given by eqs 17 and 19. Equations 16 and 21 show subtle structural differences.

If one subscribes to the hypothesis that diffusion is driven by gradients in the chemical potential (consistent with irreversible thermodynamics[9]), then eq 21 would seem to imply a chemical potential of the form:

$$\mu_i = \mu_i^0(T, P) + k_B T(\ln \phi_i + \text{constant}) \tag{22}$$

Equation 22 leads to an incorrect prediction for the osmotic pressure in the dilute-solution limit. (We recognize, however, that Bird et al.'s treatment may have been tailored to entangled melts.) In an effort to reconcile eqs 16 and 21, one may be tempted to define equivalent diffusion coefficients. For example, in one dimension one could write

$$\mathrm{D}_i = D_i[1 - \phi_i N_i(\partial\langle 1/N\rangle/\partial x)/(\partial \phi_i/\partial x)] \tag{23}$$

Equation 23, however, is inconsistent with the expectation that the transport coefficients be independent of concentration gradients in the limit of small gradients. (An exception is the case of a binary mixture, for which $\nabla\langle 1/N\rangle \propto \nabla\phi_i$, $i = 1$ or 2.)

It is interesting to compare the predictions for the binary diffusivity, $D_{12} = D_{21}$, as given by eqs 16 and 21:

$$D_{12} = k_B T\left(\frac{\phi_1}{N_2} + \frac{\phi_2}{N_1}\right)\left(\frac{\phi_1 N_2}{\xi_2} + \frac{\phi_2 N_1}{\xi_1}\right) \qquad \text{KS} \tag{24}$$

$$D_{12} = k_B T\left(\frac{\phi_1}{\xi_2} + \frac{\phi_2}{\xi_1}\right) \qquad \text{Bird et al.} \tag{25}$$

where ξ_1 and ξ_2 are those in eq 19 and KS stands for "Kramer–Sillescu". Both equations are capable of interpolating the binary diffusivity at finite concentrations and provide the correct self-diffusion limits. We are not aware of any experimental evidence that conclusively favors either eq 24 or eq 25. (The data of Jordan et al.[12] satisfactorily agreed with predictions using eq 24; this is not sufficient to guarantee that eq 24 is indeed the correct one, however.)

Equations 16, 20, and 21 are easily converted to the case of a continuous molecular weight distribution, $f(N,t,\vec{r})$, defined as:

$$f(N,t,\vec{r}) = \lim_{\Delta N \to 0} N\frac{\phi|_N^{N+\Delta}}{\Delta N} \tag{26}$$

where $\vec{r}$ and t are the position vector and time, respectively, and $\phi|_N^{N+\Delta N}$ is the mass fraction of a species with degree of polymerization between N and $N + \Delta N$. The distribution function is subject to normalization

$$\int_{-\infty}^{\infty} f(N',t,\vec{r})\, \mathrm{d} \ln N' = 1 \tag{27}$$

and the ensemble average of any MW-dependent property, $B(N)$, is obtained as:

$$\langle B\rangle(t,\vec{r}) = \int_{-\infty}^{\infty} B(N')\, f(N',t,\vec{r})\, \mathrm{d} \ln N' \tag{28}$$

If D and D are assumed to be equal and to depend only on molecular weight through eqs 17 and 19,[6,9,12,15] then eqs 20, 16, and 21 can succinctly be written as:

$$\partial f/\partial t = -\nabla \cdot \mathbf{j} \tag{29}$$

$$\mathbf{j} = -D(\nabla f - fN\nabla\langle 1/N\rangle) + f(\nabla\langle D\rangle - \langle DN\rangle\nabla\langle 1/N\rangle) \qquad \text{KS} \tag{30}$$

$$\mathbf{j} = -D\nabla f + f\nabla\langle D\rangle \qquad \text{Bird et al.} \tag{31}$$

where the functionality $D = D(N)$ is implied; we have omitted the constant density and made use of eq 28. (In the above equations N is an independent variable; hence, whereas $\langle D\rangle$, $\langle DN\rangle$, and $\langle 1/N\rangle$ are position- and time-dependent, D, DN, and N are not.) For melts of unentangled chains, where $D = D^*/N$ for all species, eq 30 becomes identical to eq 31.

Equations 29 and 30 or 31 are nonlinear and require numerical solution. Such an effort will not be attempted here. Rather, we will focus on specializing the equations to our experimental system in order to evidence some relevant features. Although we are inclined to prefer eq 30, we will use eq 31, since it is easier to manipulate and it lends itself to analytical treatment in a simplified case.

Our problem can be formulated as follows:

$$\frac{\partial f}{\partial t} = D(N)\frac{\partial^2 f}{\partial x^2} - \left(\frac{\partial f}{\partial x}\right)\left(\frac{\partial\langle D\rangle}{\partial x}\right) - f\frac{\partial^2\langle D\rangle}{\partial x^2} \tag{32}$$

$$-D(N)\frac{\partial f}{\partial x} + f\int_{-\infty}^{\infty} D(N')\frac{\partial f}{\partial x}\, \mathrm{d} \ln N' = 0 \quad \text{at } x = 0;\ \forall\, t \text{ and } N \tag{33}$$

$$f \to f^{\infty}(N) \quad \text{for} \quad x \to \infty \tag{34}$$

$$f(N, t=0, x) = f^0(N) + (f^\infty(N) - f^0(N))\,\mathbf{U}(x-\delta) \quad (35)$$

along with eq 27. In the above equations, x is the distance from the solid surface, δ is the initial thickness of the high molecular weight layer, $U(X)$ is the Heaviside step function ($U(X\leq 0) = 0$, $U(X>0) = 1$), and f^0 and f^∞ are the molecular weight distributions of the high molecular weight layer and bulk polymer, respectively.

At a first glance, eq 33 would seem to imply that the no-flux boundary condition at the surface is insufficient to guarantee a vanishing gradient. Mathematically as well as physically, however, it is in fact possible to show that $(\mathbf{j})_x = 0 \rightarrow \partial f/\partial x = 0$. Mathematical details are outlined in Appendix B. On physical grounds, recall that $(\mathbf{v}^d)_x = \partial\langle D\rangle/\partial x$ is the marker velocity of eq 12. Because the solid surface is impenetrable, $(\mathbf{v}^d)_x$ and $(\mathbf{j})_x$ must simultaneously vanish at $x = 0$, thus implying $(\partial f/\partial x)_{x=0} = 0$, $\forall N$ and t.

The above developments have two important implications. First, since D is a monotonically decreasing function of molecular mass, the marker velocity is predicted to be directed toward regions of low molecular weight, as confirmed by experiments.[6-8,12,13] Second, the vanishing gradient at $x = 0$ dictates that function f be even in x. Consequently, all odd derivatives of f and its moments (eq 28) must, at least linearly, approach zero as $x \rightarrow 0$. This feature will be exploited later on to derive an approximate solution for the near-surface MWD. (Our problem is then equivalent to the diffusive spreading over $(-\infty < x < \infty)$ of a square pulse of thickness 2δ centered at $x = 0$.)

Equation 32 is in the standard form of evolution equations from kinetic theory,[4,15,48] for which averaging methods have been developed. For a linear mixing rule (eq 1), the measured dielectric loss, $\langle\epsilon''\rangle$, reflects the following convolution (see eqs 1-3 and 4-6):

$$\langle\epsilon''\rangle/\Delta\epsilon = \int_0^\infty \Phi(\pi x/L)\,\mathrm{d}(\pi x/L)\int_{-\infty}^{\infty} f(N', x, t) \times F(\omega\tau(N'))\,\mathrm{d}\ln N' \quad (36)$$

where functions F and Φ are defined in eqs 2 and 5, respectively. It is then natural to explore the possibility of obtaining an evolution equation for the observable $\langle\epsilon''\rangle(\omega,t)$. This can be accomplished by multiplying eq 32 by $F\Phi$ and then integrating as done in eq 36. (This procedure is identical to that used to obtain evolution equations for moments of the phase-space distributions in kinetic theory.[4,15,48]) For simplicity, we consider the limit $L/\pi\delta \rightarrow 0$, where Φ can be approximated as a Dirac δ function centered at $x = 0$. (The general case of finite $L/\pi\delta$ can be as easily treated by integration by parts, but the results are less immediate.) We obtain

$$\langle\dot{\epsilon}''\rangle = \Delta\epsilon\langle DF(\omega\tau)\rangle_0^{II} - \langle\epsilon''\rangle\langle D\rangle_0^{II} \quad (37)$$

where $\dot{(\,)}$ and $(\,)^{II}$ denote differentiation once over time and twice over x, respectively. Note that we have dropped the term $-\langle\epsilon''\rangle_0^I\langle D\rangle_0^I$, for it is quadratic in x.

Equation 37 shows that the evolution of the dielectric loss at a selected frequency, ω, does not directly mirror the change in concentration of the species with relaxation time $\tau \sim \omega^{-1}$. (An exception would be the case of monodisperse type A polymers in a dielectrically inactive matrix.) Unfortunately, eq 37 is of limited use, since functions $\langle D\rangle_0^{II}(t)$ and $\langle DF(\omega\tau)\rangle_0^{II}(t)$ are not known a priori. (In fact, one can derive evolution equations for unknown moments by the same procedure used to get eq 37. The resulting equations, however, embody higher- and lower-order moments and can only be solved by ad hoc closure procedures.)

Table 1. Characteristics of *cis*-Polyisoprene Samples

sample	$M_w \times 10^{-3}$	M_w/M_n	microstructures (mol %)[a] cis-1,4	trans-1,4	vinyl-3,4	antioxidant (wt %)
PI-20	19.2	1.25	68.5	25.4	6.2	0.40[b]
PI-40	41.6	1.30	68.7	24.8	6.5	0.40[b]
Lir30	22.1	1.39	62.5	30.1	7.4	0.10[c]
Lir50	43.3	1.33	62.8	30.8	6.4	0.10[c]

[a] Determined by proton NMR. [b] Phenyl-β-naphthylamine. [c] 2,6-Di-*tert*-butyl-4-methylphenol.

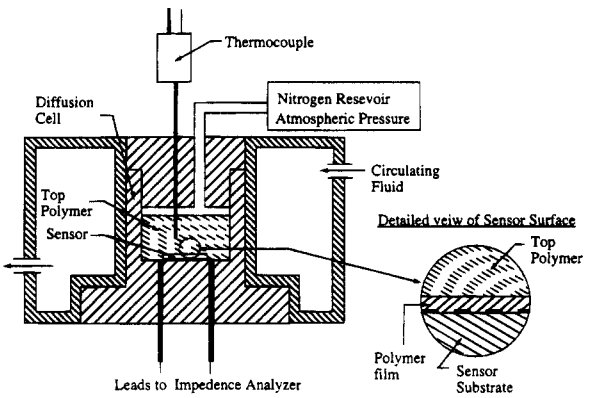

Figure 3. Schematic of the experimental setup. The sensor, precoated with a thin polymer film, rests at the bottom of the diffusion cell which serves both in containing the top polymer and as an electrical shield. The nitrogen reservoir is used to compensate for density changes in the gas during heating or cooling. The hollow external jacket serves as a heating element. The circular inset expands the configuration at the sensor surface.

Materials and Apparatus

Two polymer couples were employed in this study, namely, PI20/PI40 (system 1) and Lir30/Lir50 (system 2). Samples' characteristics are summarized in Table 1. These polymers were also used in previous studies, to which the reader may refer for full details about characterization.[31] Lir30 and Lir50 are commercially produced by Kuraray Co., Ltd., Japan, while PI20 and PI40 were synthesized anionically[49,50] in our laboratory. The commercial samples had a reported content of 0.10 wt % BHT antioxidant, while our polymers were stabilized with 0.40 wt % phenyl-β-naphthalamine, as recommended in ref 50. All samples were in the form of completely transparent, highly viscous liquids (room temperature melt viscosities ranged from 100 to 1000 [Pa s]).

The experimental setup is schematically illustrated in Figure 3. In system 1 (PI20/PI40), a 84 ± 2 μm layer of PI40 was first deposited on the sensor surface, and a large excess of melt PI20 (about 1 cm deep) was then overlaid to that film at the beginning of the experiment. In system 2, a 74 ± 1 μm layer of Lir50 was deposited, and the top "semiinfinite" medium was Lir30. (The denser, high molecular weight polymers were always placed at the bottom to avoid possible buoyancy-driven flow. This measure was overly cautious, since density differences between the melts are extremely small.) In all cases extreme care was taken to avoid entrainment of air bubbles and ensure complete wetting of the sensor. (The absence of air bubbles in the bottom layer was confirmed by microscopy.)

High molecular weight polymer films were deposited as follows. Samples were diluted with HPLC-grade toluene to yield a viscosity of about 15 Pa s at 22 °C. The solution was spin-coated on the sensor at 1700 rpm for about 2 min, and the film was then vacuum-dried at room temperature (22 °C) for 1 day. Layer thicknesses were measured by microscopy (Nikon Optiphot2-Pol polarizing microscope) with a calibrated z-stage (1 μm/division) at 200×. Because the polymer is

transparent, a minute amount of water droplets (about 10 μm in diameter) was deposited on the film by breathing on it; the drops rapidly evaporated within about 20 s. The droplets were focused on immediately prior to complete evaporation. Film thicknesses were determined by in turn focusing on the drops and then the gold electrodes at the sensor surface and recording the differences in heights of apparent focal points. The data were corrected for "virtual image" effects due to refraction with Fresnel law and the measured refractive index of the film ($n = 1.52$) and objective parameters. (This method was verified on thin glass slides of known thickness and refractive index. The corrected optical thicknesses agreed with micrometer measurements within 2%.) Several measurements were taken over the entire sensor area to inspect film thickness uniformity; standard deviations of 1.9 and 1.0 μm in uniformity were recorded in systems 1 and 2, respectively. Height measurements by microscopy were verified on polystyrene microspheres with a known diameter of 50 ± 2.5 μm (the uncertainty reflects particle-to-particle variance). Measurements repeated on the same particles by different operators were reproducible to within ±1 μm.

Immediately following deposition of the "bulk" polymer on the sensor-layer assembly (at room temperature), the diffusion cell was sealed under dry nitrogen (Figure 3) and then brought to 97 ± 0.5 °C. Temperature was controlled by encasing the cell in an externally insulated, hollow metal jacket through which an ethylene glycol/water mixture was flown from a thermostatic recirculator. The elapsed time between overlaying the bulk polymer, sealing the cell, and fitting the thermal jacket was about 10 min, after which full thermal equilibration of the bulk polymer to 97 °C required about 1 h. Therefore, the uncertainty in the time origin is estimated to be about 1 h. (This estimate is conservative, since the time–temperature shift factor undergoes a 38-fold change between 22 and 97 °C.[27,28,31])

Dielectric measurements were performed with a Hewlett-Packard 4284A impedance analyzer, at a test voltage of 100 mV (peak-to-peak). The nominal frequency range of the instrument is 20 Hz to 1 MHz, but the noise becomes significant below 200 Hz. Acquisition of each spectrum required about 15 min. All electrical connections were shielded, and leads were kept as short as possible (~50 cm coaxial cable, ~1.2 pF/cm) to minimize stray impedances.

Dielectric loss spectra of *cis*-PI obey time–temperature superposition.[24-28,31] The use of a high temperature was required to shift the spectra to high frequencies, thereby exposing a larger portion of the low-frequency side of the peaks. Unfortunately, prolonged exposure to a harsh thermal environment can cause degradation and cross-linking of the samples. Signs of incipient degradation were detected in the PI20/PI40 system after about 17 h from the beginning of the experiment. At longer times, the MWDs obtained by inversion showed an anomalous enrichment of low molecular weight material near the surface. Initially, these trends were not attributed to degradation, although suspicions became strong after about 1 week of the treatment. The trends were so peculiar that the experiment was continued for 4 weeks, at which time the high-frequency side of the spectra had disproportionately outgrown that of the final expected one of PI20. The brown, rubbery appearance of the material ultimately extracted from the cell confirmed the occurrence of extensive cross-linking and degradation. By contrast, the Lir30/Lir50 system showed very few signs of degradation. Up to 10 days the spectra and the inversions did not exhibit any sign of material deterioration. Upon terminating the experiment the sample showed a light yellowish color, but no evident signs of cross-linking. The differences in degradation behavior between PI20/PI40 and Lir30/Lir50 can most likely be attributed to the different antioxidants (Table 1).

Results and Discussion

The evolving loss spectra of systems 1 (PI20/PI40) and 2 (Lir30/Lir50) are shown in Figures 4 and 5, respectively. To avoid crowding the figures, only selected spectra are displayed along with the self-consistent fits.

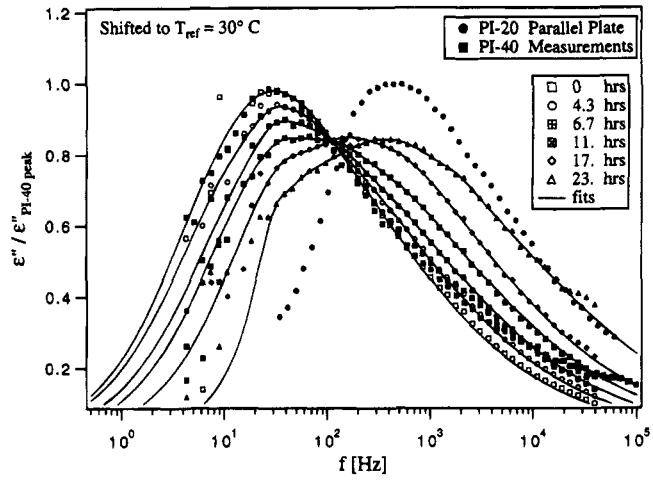

Figure 4. Evolution of the near-wall dielectric loss during diffusion for system 1. The curves are normalized by the peak value for PI40. All spectra have been shifted to a reference temperature of 30 °C. Time from the beginning of the experiment is indicated in the legend. The filled symbols indicate parallel-plate measurements for pure PI20 and PI40. The lines are self-consistent fits of the spectra as described in ref 32.

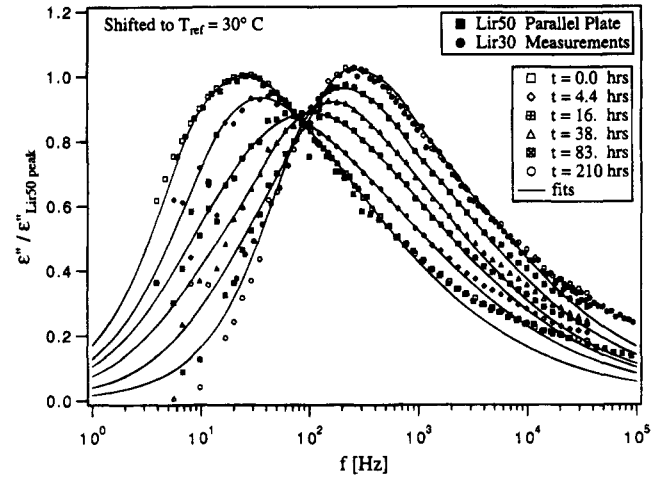

Figure 5. Evolution of the near-wall dielectric loss during diffusion for system 2. The curves are normalized by the peak value for PI40. All spectra have been shifted to a reference temperature of 30 °C. Time from the beginning of the experiment is indicated in the legend. The filled symbols indicate parallel-plate measurements for pure Lir30 and Lir50. The lines are self-consistent fits of the spectra as described in ref 32.

(Recall that in Figure 4 only the first 17 h of the experiment may be meaningful.) Both systems exhibit similar trends. Starting from the spectrum of the high molecular weight film at $t = 0$, the loss peaks gradually shift to higher frequencies, reflecting enrichment in the near-surface region of small chains. Noteworthy is the fact that all curves pivot about the frequency where the initial and final spectra cross. The significance of this finding will become clear later on. The long-time spectrum of system 2 (Figure 5) matches fairly well that of Lir30. This suggests that degradation was a minor effect for this couple (although, some deterioration in the final stages of the experiment cannot be ruled out with certainty).

The time-dependent MWDs obtained by inversion of the spectra are displayed in Figures 6 (system 1) and 7 (system 2). Again, only selected curves are shown. In Figure 8 we have plotted the entire inversion data set for the Lir30/Lir50 system, to illustrate the resolution

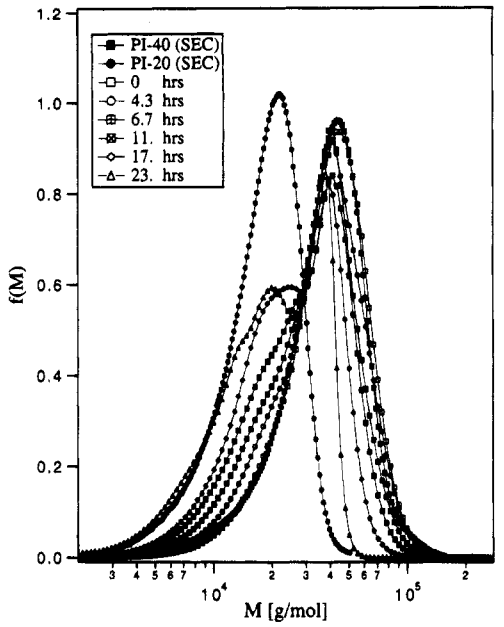

Figure 6. Evolution of the near-wall molecular weight distribution during diffusion for system 1 obtained from inversion of loss spectra. Time from the beginning of the experiment is indicated in the legend. The filled symbols indicate SEC data for pure PI20 and PI40. The molecular weight distributions are expressed as $f(M) = \phi(M)/\Delta \ln M$.

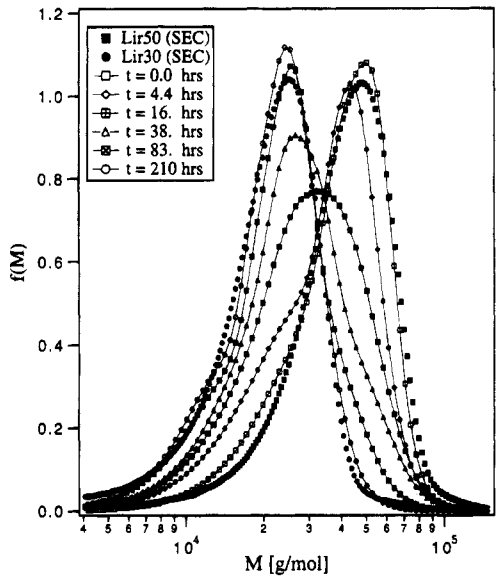

Figure 7. Evolution of the near-wall molecular weight distribution during diffusion for system 2 obtained from inversion of loss spectra. Time from the beginning of the experiment is indicated in the legend. The filled symbols indicate SEC data for pure Lir30 and Lir50. The molecular weight distributions are expressed as $f(M) = \phi(M)/\Delta \ln M$.

of the technique. (Note that the curves are not all evenly spaced in time.) Figures 6–8 more effectively portray the trends deduced by analysis of the loss spectra. The near-surface concentration of high molecular weight chains drops rapidly as the distribution gradually develops a shoulder on the low molecular weight side, while pivoting about the point where the initial and final MWDs cross.

Figure 9 displays the evolution of the dielectric loss for system 2 at selected frequencies. The values of 24 and 258 Hz (with spectra shifted to $T_{ref} = 30$ °C) roughly correspond to the peaks of the zero- and infinite-time spectra, respectively, while 86 Hz corresponds to the "pivoting" frequency. Evolution of the concentration of

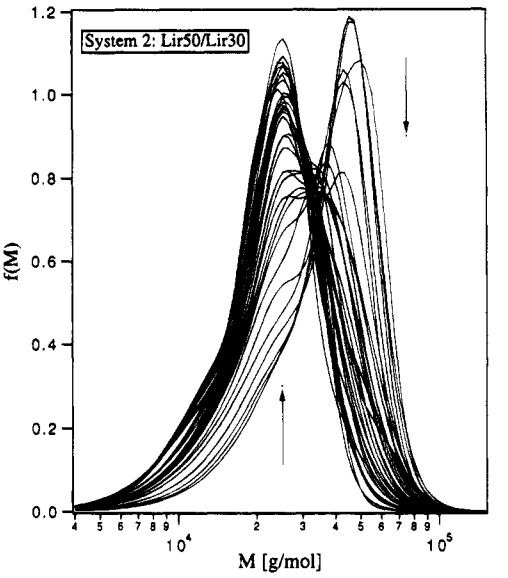

Figure 8. Evolution of the near-wall molecular weight distribution during diffusion for system 2 obtained from inversion of loss spectra. All the acquired isochronal curves are shown to illustrate the resolution of the technique. (Note that the curves are not all evenly spaced in time.) The arrows indicate the direction of evolution of the distribution over time.

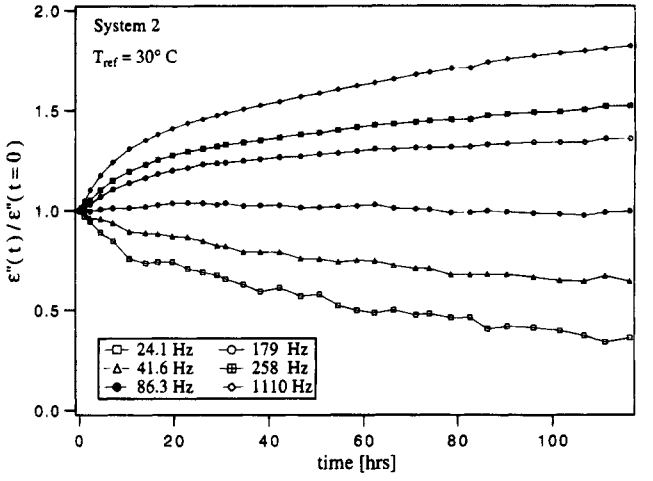

Figure 9. Evolution of the dielectric loss normalized by initial values for system 2 at selected frequencies (shifted to T_{ref} = 30 °C). The values of 24 and 258 Hz roughly correspond to the peaks of the zero- and infinite-time spectra, respectively, while 86 Hz corresponds to the "pivoting" frequency as described in the text.

individual species can be followed by focusing on selected molecular weights in Figures 6 and 7. In Figure 10 we have plotted the normalized mass fractions, $f(M,t)/f(M,t=0)$, against time for the species with relaxation time equal to the inverse of the peak and pivoting frequencies of Figure 9. Although showing similar trends, the curves in Figures 9 and 10 do not exhibit direct correspondence. This finding conforms to the conclusions reached in connection with eq 37.

The significance of the pivoting frequency (Figures 4 and 5) can be clearly understood by examining Figures 6 and 7. The frequency of 86 Hz (system 2) corresponds to the point where the initial and final MWDs cross ($M_+ \sim 32\,000$). For such species no concentration gradient exists to begin with, so that diffusional rearrangement is expected to be a secondary effect, controlled by the gradient in the marker velocity (eqs 12 and 32) ($\mathbf{v}^d$ is zero at the surface).

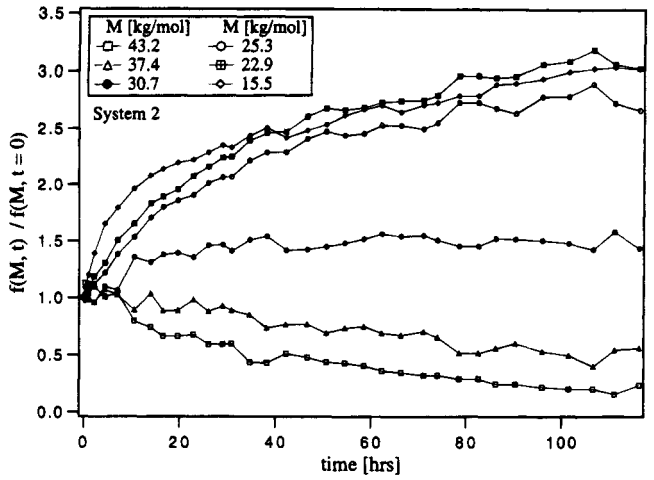

Figure 10. Normalized mass fractions against time for the species with relaxation time equal to the inverse of the peak and pivoting frequencies of Figure 9.

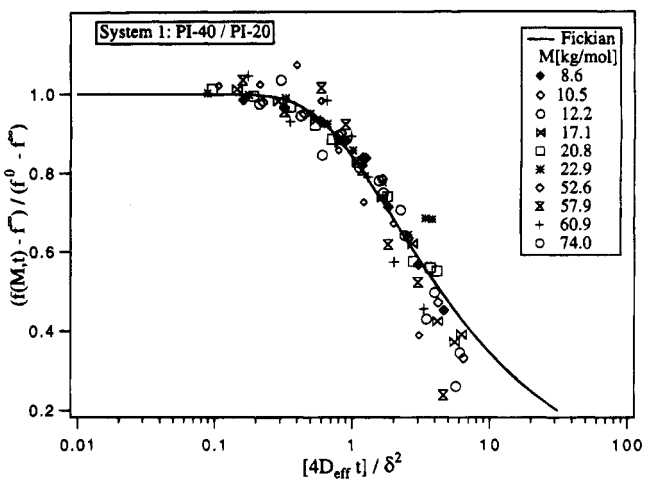

Figure 11. Normalized mass fractions (eq 40) against dimensionless time (eq 42) for system 1. The data for different molecular weights have been logarithmically shifted from real time to achieve superposition with the Fickian curve (eq 44).

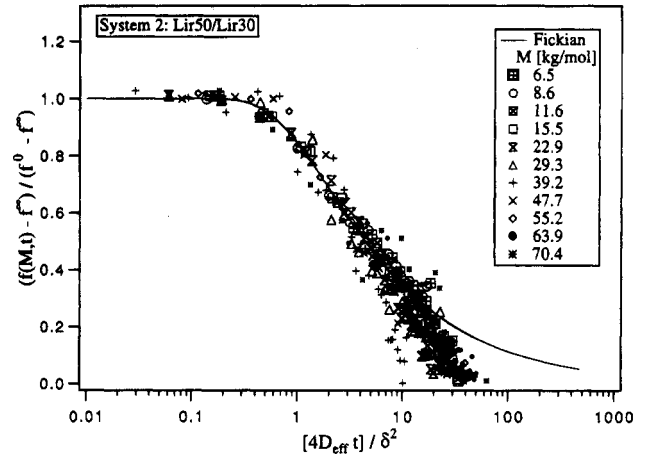

Figure 12. Normalized mass fractions (eq 40) against dimensionless time (eq 42) for system 2. The data for different molecular weights have been logarithmically shifted from real time to achieve superposition with the Fickian curve (eq 44).

Data analysis with the equations derived in the theoretical section is an onerous undertaking, which requires a separate, careful numerical study. As a first-order approximation the data can be analyzed by assuming Fickian diffusion with a molecular weight dependent effective diffusivity, $D_{\text{eff}}(M)$. Of course, we realize the fallacy of this postulate from the start, for we are deliberately ignoring mass balance constraints (eq 11). Also, the shape of the experimental profiles will not be strictly Fickian. On the other hand, a simple analysis should allow us to rationalize main trends in the data and provide guidance for future numerical studies. We first present the results and then discuss the implications of the assumptions.

In terms of the continuous MWD, the problem simplifies to:

$$\frac{\partial f}{\partial t} = D_{\text{eff}}(N)\frac{\partial^2 f}{\partial x^2} \tag{38}$$

$$\partial f/\partial x = 0 \quad \text{at} \quad x = 0;\ \forall\, t \text{ and } N \tag{39}$$

along with the initial and boundary conditions given by eqs 34 and 35; $D_{\text{eff}}(N)$ is the effective diffusivity. The equations are nondimensionalized as follows:

$$u^* = (f - f^\infty)/(f^0 - f^\infty) \tag{40}$$

$$x^* = x/\delta \tag{41}$$

$$t^* = 4D_{\text{eff}}t/\delta^2 \tag{42}$$

and the solution is[51]

$$u^* = \frac{1}{2}\left\{\text{erf}\left(\frac{1 - x^*}{t^{*1/2}}\right) + \text{erf}\left(\frac{1 + x^*}{t^{*1/2}}\right)\right\} \tag{43}$$

where erf( ) is the error function. For $L/\pi\delta \ll 1$ the near-surface composition is essentially constant and we can set $x^* = 0$, giving

$$u^* = \text{erf}(1/t^{*1/2}) \tag{44}$$

The effective diffusivity, $D_{\text{eff}}(M)$, is obtained by logarithmically shifting the data for each molecular weight along the time axis to achieve superposition with the theoretical $u^*(t^*)$ curve and then using eq 42 with the known value of δ ($\delta = 84$ μm for system 1 and $\delta = 74$ μm for system 2). To reduce the influence of degradation, shifting was implemented by focusing primarily on the small-times portion of the curves. The results are displayed in Figures 11 (system 1) and 12 (system 2). The Fickian prediction captures reasonably well the main trends in the data at small times. At longer times deviations become appreciable, and the decay is much faster than the predicted $t^{-1/2}$ dependence. This result should be considered carefully, since the long times data are likely to be affected by degradation.

The effective diffusivities for systems 1 and 2 are logarithmically plotted against molecular weight in Figure 13. The results from both systems are comparable. This is not surprising, considering similarities between samples Lir30–PI20 and Lir50–PI40. The molecular weight dependence of D_{eff} is quite complex. Starting from an apparently constant value at low molecular weights, the data drop by nearly 1 order of magnitude above the critical molecular weight for entanglement ($M_c \sim 10\,000$) and then rise again above $M_+ \sim 32\,000$, to finally approach a value comparable to the low molecular weight limit. (The data below 10 000 and above 70 000 are likely to be highly inaccurate, since there, inversion errors are significant.) Interestingly, between 10 000 and 30 000, the data seem to follow a power law with a slope −2, consistent with the

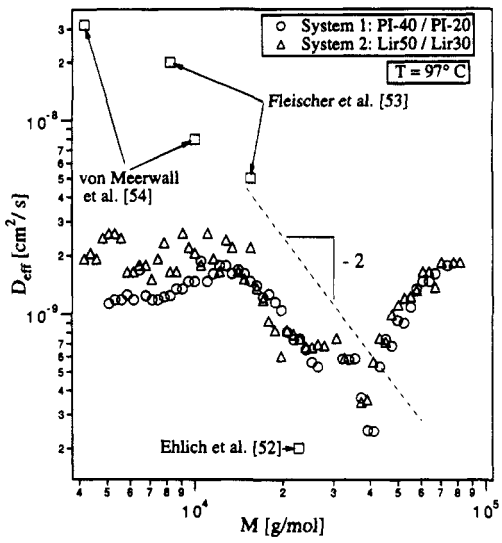

Figure 13. Effective diffusivities, D_{eff}, against molecular weight for both system 1 and system 2, plotted along with the data of Ehlich et al.,[52] Fleischer et al.,[53] and Von Meerwall et al.[54] for self-diffusion in *cis*-PI melts. A reference line of slope of −2 is also plotted (dashed line).

scaling from reptation theory. Caution should be exerted in evaluating this finding, since the error bars are quite large and the model used to obtain D_{eff} is rather crude. Plotted in Figure 13 are also the tracer diffusivities of Elhich et al.,[52] Fleischer et al.,[53] and Von Meerwall et al.[54] (the data were reduced to our temperature). The points are scattered, and our data fall in an intermediate range.

The molecular weight where the diffusivity shows an upturn in Figure 13 is close in value to the one where the zero- and infinite-time MWDs cross in Figure 7. We do not believe this to be a coincidence. In binary systems Kramer et al.[6] and other authors[7,8] have shown that the high molecular weight side of a diffusion couple will swell at a rate dictated by the penetration of the smaller chains. The initial concentration profile in our system is such that, for species with $M < M_+$, diffusion occurs toward the sensor surface, while for $M > M_+$ transport is in the opposite direction. Expansion of the high molecular weight layer, caused by an inward rush of small chains, will then displace large, slowly-diffusing species away from the sensing area. For $M > M_+$ diffusion and convection occur in the same direction, so that the effective diffusivity is either exaggerated or completely dominated by convection. For $M < M_+$ diffusion and swelling occur in opposite directions, and the apparent diffusion coefficients are somewhat diminished in magnitude. Mass balance constraints force the convective time scale of the large chains to be comparable to that for cumulative diffusion of the small species toward the surface. The rate-limiting step is then diffusion of the small chains toward the wall. The trends in Figure 13 are consistent with these expectations. (Incidentally, we should mention that calculation of D_{eff} in the neighborhood of M_+ is very difficult, since, there, changes in composition are minimal. Consequently, errors become quite large as M approaches M_+. This is the reason for the fewer data points in the crossover region in Figure 13.)

A Simplified Treatment

Solution of eqs 32−35 is very difficult, generally requiring numerical methods. An analytical solution for the near-surface ($x = 0$) MWD can be obtained for a simplified version of the Bird et al. model that takes advantage of the particular structure of our system. Recall that the no-flux boundary condition at $x = 0$ endows $f(N,t,x)$ with an even functionality on x. From eqs 28, 32, and A2 (Appendix A) we obtain, around $x^* \sim 0$:

$$\langle D\rangle(t,x^*) = \int_{-\infty}^{\infty} D(N')\, f_0(t,N')\, \mathrm{d}\ln N' + \frac{x^{*2}}{2!}\int_{-\infty}^{\infty} D(N')\, f_0^{\mathrm{II}}(t,N')\, \mathrm{d}\ln N' + O(x^{*4}) \quad (45)$$

$$\langle D\rangle^{\mathrm{II}} \approx \int_{-\infty}^{\infty} D(N')\, f_0^{\mathrm{II}}(t,N)\, \mathrm{d}\ln N' + O(x^{*2}) \quad (46)$$

$$\langle D\rangle^{\mathrm{I}} f^{\mathrm{I}} \approx O(x^{*2}) \quad (47)$$

where again the Roman numerals denote differentiation with respect to $x^* = x/\delta$, and the subscript "0" stands for "evaluated at $x = 0$". We now ignore terms of order x^{*2} and approximate eq 32 as:

$$\frac{\partial f}{\partial t} = D(N)\frac{\partial^2 f}{\partial x^2} - f\,\Omega(t) \quad (48)$$

$$\Omega(t) \equiv \int_{-\infty}^{\infty} D(N')\left(\frac{\partial^2 f}{\partial x^2}\right)_{x=0} \mathrm{d}\ln N' \quad (49)$$

subject to

$$\int_{-\infty}^{\infty} f(N',t,0)\, \mathrm{d}\ln N' = 1 \quad (50)$$

and eqs 34, 35, and 39. We have reverted the notation back to x, since there is no advantage in using x^*. Function $\Omega(t)$ is not known a priori and must be determined in a self-consistent manner from eq 49.

We must emphasize that eq 48 is strictly valid only at the origin. Rigorously, a perturbation expansion in x^* should have included also f and the cross term (eq 47), resulting in an infinite set of coupled differential equations in time for terms of like order in x. Therefore, our treatment hinges not on a simplified form of the equations but, rather, on a "simplistic" (and hopefully realistic) version of them. Nevertheless, eqs 48−50 improve over the pseudo-Fickian model (eq 38), in that they retain mass balance constraints at the surface (eq 50). Although we solve them over the entire range ($0 \le x < \infty$), we recognize that the solution will be meaningful only at $x = 0$, as reflected by eq 50.

Equations 48−50 admit the following solution

$$f(N,t,x) = H(t)\, G(N,t,x) \quad (51)$$

$$H(t) = \exp\left(-\int_0^t \Omega(t')\, \mathrm{d}t'\right) \quad (52)$$

$$G(N,t,x) = A(N) + B(N)\, u(N,t,x) \quad (53)$$

$$u(N,t,x) \equiv \frac{1}{2}\left\{\mathrm{erf}\left(\frac{\delta - x}{(4D(N)\,t)^{1/2}}\right) + \mathrm{erf}\left(\frac{\delta + x}{(4D(N)\,t)^{1/2}}\right)\right\} \quad (54)$$

where functions $A(N)$ and $B(N)$ remain to be determined. It can be seen that the solution is characterized by two time scales, namely, one based on the diffusivity of the species ($\delta^2/4D(N)$) and the other dependent on the average diffusion coefficient ($\sim\delta^2/\langle D\rangle$) through Ω in eq 49. In particular, for $\langle D\rangle/D(N) \gg 1$, function $H(t)$ controls the evolution, while, for $\langle D\rangle/D(N) \ll 1$, the

Fickian term dominates. In essence, transport of large chains is controlled by the average diffusivity, whereas small chains essentially obey Fickian diffusion. These features are in qualitative agreement with the trends in Figure 13.

We now go on to the task of determining function $\Omega(t)$. To simplify the notation, we let

$$[[g]](t,x) \equiv \int_{-\infty}^{\infty} g(N',t,x)\, \mathrm{d} \ln N' \tag{55}$$

From eqs 48, 49, and 51 we obtain

$$\Omega(t) = \Theta(t) \exp(-\int_0^t \Omega(\tau)\, \mathrm{d}\tau) \tag{56}$$

where

$$\Theta(t) \equiv \left[\left[D\left(\frac{\partial^2 G}{\partial x^2}\right)_{x=0}\right]\right] = \left[\left[\left(\frac{\partial G}{\partial t}\right)_{x=0}\right]\right] = \left(\frac{\partial [[G]]}{\partial t}\right)_{x=0} \tag{57}$$

Differentiation of eq 56 in time produces

$$\frac{\mathrm{d}\Omega}{\mathrm{d}t} = \frac{\mathrm{d} \ln \Theta}{\mathrm{d}t}\Omega - \Omega^2 \tag{58}$$

which is separable and can be solved to give

$$\Omega(t) = \frac{\Theta(t)}{C + \int_0^t \Theta(t')\, \mathrm{d}t'} = \frac{\mathrm{d}}{\mathrm{d}t} \ln\{C + [[G]](t,0) - [[G]](0,0)\} \tag{59}$$

where C is a constant. Substituting eq 59 in eqs 51–54 and setting $x = 0$, we obtain

$$f(N,t,0) = \frac{A(N) + B(N)\, u(N,t,0)}{C - [[G]](0,0) + [[A(N)]] + [[B(N)\, u(N,t,0)]]} \tag{60}$$

Imposition of eqs 50, 34, and 35 leads to $C = [[G]](0,0)$ and

$$f(N,t,0) = \frac{f^{\infty}(N) + (\xi f^0(N) - f^{\infty}(N))\, u(N,t,0)}{1 + [[(\xi f^0(N) - f^{\infty}(N))\, u(N,t,0)]]} \tag{61}$$

where $\xi = 1 + [[B(N)]]/[[A(N)]]$. If ξ is assumed to be independent of moments of f^0 and f^{∞}, then the limiting case $f^0(N) \to f^{\infty}(N) \Rightarrow f \to f^{\infty}(N)$ mandates that $\xi = 1$. Equation 61 satisfies eq 50 for arbitrarily assigned $f^0(N)$, $f^{\infty}(N)$, and $D(N)$.

We must point out an inconsistency that emerges upon manipulating eq 48. If we apply the operator in eq 55 to eqs 48 and 61 at $x = 0$, we find

$$\left[\left[\frac{\partial f}{\partial t}\right]\right]_{x=0} = \left[\left[D(N)\frac{\partial^2 f}{\partial x^2} - f\Omega(t)\right]\right]_{x=0} = 0 \tag{62}$$

$$[[f(N,t,x)]]_{x=0} = 1 \tag{63}$$

as it should be. However, if we rearrange eq 48 to isolate the second derivative and then apply eq 55 and eqs 51–54, we obtain

$$\left[\left[\left(\frac{\partial^2 f}{\partial x^2}\right)_{x=0}\right]\right] = \left[\left[\frac{1}{D(N)}\left(\frac{\partial f}{\partial t} + f\Omega(t)\right)_{x=0}\right]\right] = H(t)\left[\left[\frac{\partial G/\partial t|_{x=0}}{D(N)}\right]\right] \neq 0 \tag{64}$$

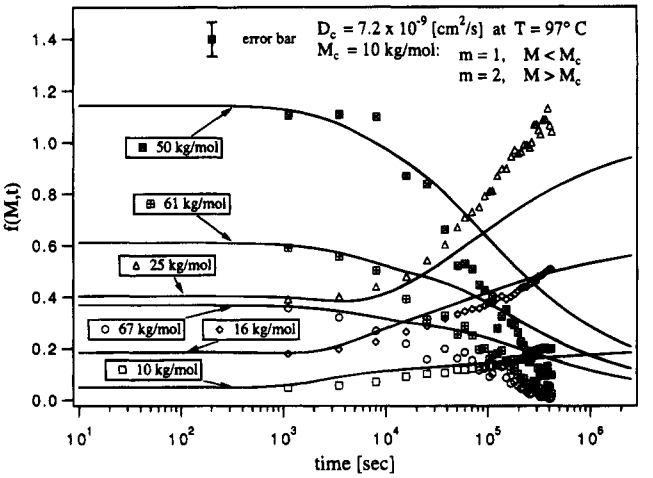

Figure 14. Molecular weight distribution data against time for system 2 (symbols) compared to the simplified model (lines) of eq 61. Molecular weights for each curve and model parameters are indicated. The bar at the top left corner provides an estimate of the absolute error in the data.

which is incorrect. The implications of this finding are not obvious, but we believe the restriction of a vanishing average curvature to be less stringent than eqs 62 and 63.

In order to compare the predictions of eq 61 to our data, the molecular weight dependence of $D(N)$ must be assigned ($f^0(N)$ and f^{∞}(N) are known from inversion of the spectra as well as SEC measurements). We assume the following functionality:

$$D(M) = D_c(M_c/M)^m; \quad m = 1 + U(M/M_c - 1) \tag{65}$$

where D_c is the diffusion coefficient at M_c = 10 000 (double the entanglement molecular weight of *cis*-PI[31,35]) and $U(X)$ the Heaviside step function. Equation 65 overestimates the diffusivity around M_c but is a reasonable first-order approximation. Parameter D_c was adjusted to yield the best visual fit of a few arbitrarily selected curves (therefore, no optimization was applied). The results for system 2 (Lir30/Lir50) are shown in Figure 14 (the value of D_c is reported in the figure).

The model captures reasonably well the evolution of the low molecular weight species up to about 24 h but gives very poor results for the high molecular weight fractions. Above 24 h departures are considerable, as for the pseudo-Fickian case of Figures 11 and 12, again indicating that sample degradation may have played a role.

The predicted and experimental MWDs at selected times are compared in Figure 15a,b. The most noticeable feature is the model's inability to capture the rapid diffusion of the large chains. We were concerned that such a discrepancy might have in part been due to inversion errors. The predicted MWDs were thus converted to loss spectra using eqs 1–3. The results are compared to the experimental spectra in Figure 16a,b. Again, the decay of the spectra at low frequencies (large chains) is much too sluggish. The inability of our simplistic model to capture the experimental behavior is confirmed. Whether such trends can be attributed to model failure or sample degradation remains to be established. Further experiments and numerical solution of the Kramer–Sillescu equations are currently being considered.

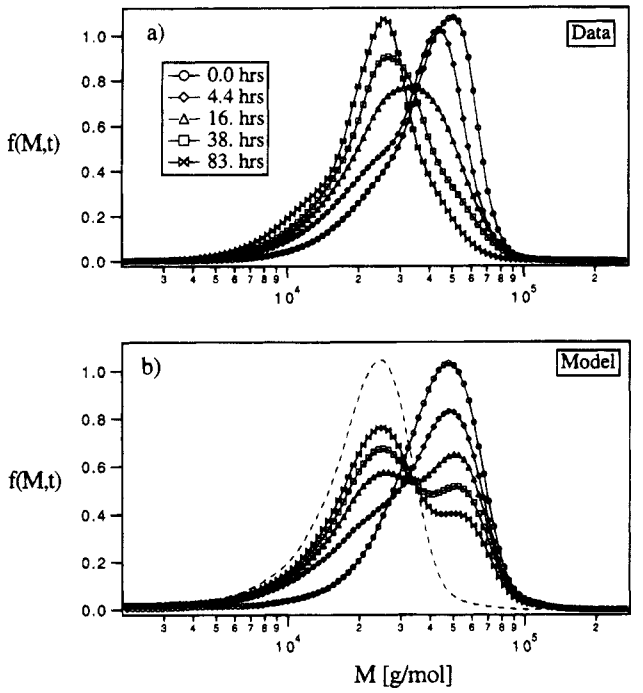

Figure 15. Molecular weight distributions from inversions of loss spectra (a) compared to model predictions (b) (eq 61), at the times noted in the legend.

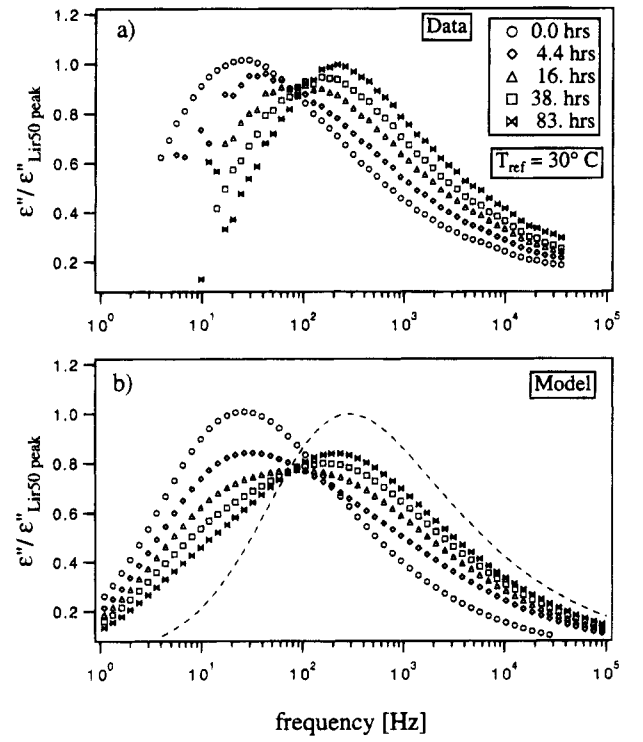

Figure 16. Experimental loss spectra (a) compared to model predictions (b) (from eq 61 and eqs 1–3), at the noted times. The curves are referenced to the peak value of the Lir50 spectrum.

Conclusion

We have demonstrated the use of normal-mode microdielectrometry to monitor multicomponent diffusion in polydisperse *cis*-PI melts. We have also proposed an extension of the Kramer–Sillescu theory to polydisperse systems. The constitutive equations for the fluxes have been compared to those obtained by Bird et al. from kinetic theory. Both theories are plausible, and available evidence is insufficient to conclusively favor either.

Data analysis relied on a simple Fickian model, with a molecular weight dependent effective diffusivity. Consistent with previous studies on binary systems, we find that diffusive penetration of smaller chains causes a net swelling of the high molecular weight polymer. Large chains are displaced at a rate dictated by the penetration of small molecules. As a consequence, the effective diffusivity drops by nearly 1 order of magnitude above the entanglement molecular weight, $M_c \approx 10\,000$, and then rises again to approach a value comparable to that of the small chains. Trend reversal occurs at $M_+ \approx 32\,000$, where the final and initial MWDs cross. Between M_c and M_+ the data exhibit a power-law dependence with an exponent close to -2 (although, experimental error and possible sample degradation make this value highly uncertain).

An analytical solution for the time evolution of the near-surface MWD has been obtained from a simplified version of the Bird et al. model. Although the main trends are correct, quantitative comparison with the experiments is poor, especially at long times. Sample degradation and/or model failure could be responsible for this discrepancy. Experiments of shorter duration, with more stable samples, thinner films, and sensors with shorter penetration depth, as well as numerical studies should help clarify this issue.

We conclude by addressing a potential point of concern. It is now well established[24–28,31–32,35] that a quantitative description of dielectric and mechanical loss spectra of *cis*-PI requires a 3.7 power law dependence of the relaxation time, τ, on molecular weight, M. Indeed, the results of the present work hinge entirely on such a premise. The prediction of reptation theory, $\tau \sim M^3$, deviates but is not far removed from the experimental 3.7 power law used to invert the spectra. Reptation theory also directly links diffusivity and relaxation time, giving $D \sim M^{-2}$. It is then natural to suspect some circularity of our argument leading from the inversion of loss spectra assuming reptation with $\tau \sim M^{3.7}$ to a (seemingly) M^{-2} dependence of the experimental diffusivity. We do not believe such a circularity to exist, for, while the inversions relied on manipulations in frequency space, the diffusivities were obtained from time-domain data. Spectral analysis and time evolution of the spectra are entirely independent processes.

Acknowledgment. The donors of the Petroleum Research Fund, administered by the American Chemical Society (Grant ACS-PRF24927-G7B), and the National Science Foundation (Grant CTS-9208478) are gratefully acknowledged for supporting this research.

Appendix A

In this section, we estimate errors due to composition inhomogeneity over the field penetration depth. For simplicity, we use the continuous molecular weight distribution, $f(N,t,x^*)$, where $x^* = x/\delta$, δ being the thickness of the high molecular weight layer. As discussed in the text (eq 36), the measured dielectric loss, $\langle\epsilon''\rangle$, reflects the following convolution

$$\langle\epsilon''\rangle/\Delta\epsilon = \int_0^\infty \Phi(\pi x/L)\, \mathrm{d}(\pi x/L) \int_{-\infty}^{\infty} f(N,t,x/\delta) \times F(\omega\tau(N))\, \mathrm{d}\ln N \quad \text{(A1)}$$

where $\tau(N)$, $F(\omega\tau)$, and Φ are given by eqs 3, 2, and 5, respectively. Function $f(N,t,x^*)$ is even in x^* and can

be expanded about the origin to give

$$f(N,t,x^*) = f(N,t)_0 + f_0^{II}(N,t)\, x^{*2}/2! + f_0^{IV}(N,t)\, x^{*4}/4! + \ldots, \quad \text{for } x^* \to 0 \quad \text{(A2)}$$

Combining eqs A1 and A2, we obtain

$$\langle \epsilon'' \rangle / \Delta\epsilon = \sum_{\substack{n=0 \\ n=\text{even}}}^{\infty} I_n(\omega)\, (L/\pi\delta)^n \quad \text{(A3)}$$

where

$$I_n(\omega) = \frac{1}{n!}\{\int_0^\infty \Phi(\xi)\, \xi^n \, d\xi\} \left\{\int_{-\infty}^{\infty} F(\omega\tau(N)) \left(\frac{\partial^n f}{\partial x^{*n}}\right)_{N,t,x^*=0} d \ln N\right\} \quad \text{(A4)}$$

and $\xi = (\pi x/L)$. We see that $|I_{n+2}| < |I_n|$, so that, to second order:

$$\langle \epsilon'' \rangle / \Delta\epsilon = I_0(\omega) + I_2(\omega)\, (L/\pi\delta)^2 + O(I_4(\omega)\, (L/\pi\delta)^4) \quad \text{(A5)}$$

In our experiments $(L/\pi\delta)^2 \sim 0.03$, so that an error of at most 3% is expected. This estimate represents an upper bound, for swelling of the near-surface layer will relieve the curvature at the origin as time progresses, thereby rendering the error even smaller.

Appendix B

The following discussion parallels the treatment of the Stefan–Maxwell equations for dilute gases.[55] We consider the model of Bird et al.[15] discretized to L mass fractions and show that the condition that the surface-normal components of the fluxes, $(\mathbf{J}_i)_n$, be zero at a solid surface leads to vanishing normal components of the concentration gradients for all species, $(\nabla\phi_i)_n$.

The equations are succinctly written as

$$(\mathbf{J}_i)_n = (\delta_{ij}D_j - \phi_i D_j)(\nabla\phi_j)_n; \quad i,j \in (1, L) \quad \text{(B1)}$$

where δ_{ij} is the Kronecker delta, ∇ is the gradient operator, ϕ_i and D_i are the volume fractions and diffusion coefficients of species i, respectively, and summation over repeated indices is implied. Note that at a solid surface $\bar{\mathbf{v}} = 0$. From the conditions

$$\sum_{k=1}^{L} \mathbf{J}_k = 0 \quad \text{(B2)}$$

$$\sum_{k=1}^{L} \phi_k = 1 \quad \text{(B3)}$$

it follows that only $L - 1$ equations are linearly independent. Eliminating the equation for component L, using eq B3, and setting $(\mathbf{J}_i)_n = 0$ at the solid surface $\forall\ i$, we obtain the following homogeneous system of equations:

$$K_{ij}(\nabla\phi_j)_n = 0; \quad i,j \in (1, L-1) \quad \text{(B4)}$$

where

$$K_{ij} \equiv (\delta_{ij}D_j - \phi_i(D_j - D_L)) \quad \text{(B5)}$$

Equation B4 requires that either $\det(K_{ij}) = 0$ or $(\nabla\phi_i)_n = 0$ $(\forall i)$. The determinant of K_{ij} is

$$\det(K_{ij}) = \prod_{i=1}^{L-1} D_i - \sum_{i=1}^{L-1} \phi_i (D_i - D_L) \prod_{j=1; j\neq i}^{L-1} D_j \quad \text{(B6)}$$

Straightforward manipulation of eq B6 subject to eq B3 gives

$$\det(K_{ij}) = \phi_L \prod_{i=1}^{L-1} D_i + \sum_{i=1}^{L-1} \phi_i \prod_{j=1; j\neq i}^{L} D_j \quad \text{(B7)}$$

Clearly, for physically meaningful values of D_i and ϕ_i, $\det(K_{ij}) \neq 0$. Therefore, at a solid surface, $(\nabla\phi_i)_n = 0\ \forall\ i \in (1, L)$.

References and Notes

(1) Tulig, T. J.; Tirrell, M. *Macromolecules* **1981**, *14*, 1501.
(2) Wu, S. *Polymer Interface and Adhesion*; Dekker: New York, 1982.
(3) Kausch, H. H.; Tirrell, M. *Annu. Rev. Mater. Sci.* **1989**, *19*, 341.
(4) Doi, M.; Edwards, S. F. *The Theory of Polymer Dynamics*; Oxford University Press: New York, 1989.
(5) de Gennes, P.-G. *J. Chem. Phys.* **1971**, *55*, 572.
(6) Kramer, E. J.; Green, P.; Palmstrom, C. J. *Polymer* **1984**, *25*, 473.
(7) Liu, Y.; Reiter, G.; Kunz, K.; Stamm, M. *Macromolecules* **1993**, *26*, 2134.
(8) Reiter, G.; Hüttenbach, S.; Foster, M.; Stamm, M. *Macromolecules* **1991**, *24*, 1179.
(9) Sillescu, H. *Makromol. Chem., Rapid Commun.* **1987**, *8*, 393.
(10) Sillescu, H. *Makromol. Chem., Rapid Commun.* **1984**, *5*, 519.
(11) Brochard, F.; Jouffroy, J.; Levinson, P. *J. Phys. Lett.* **1983**, *44*, 455.
(12) Jordan, E. A.; Ball, R. C.; Donald, A. M.; Fetters, L. J.; Jones, R. A. L.; Klein, J. *Macromolecules* **1988**, *21*, 235.
(13) Composto, R. J.; Kramer, E. J.; White, D. M. *Nature* **1987**, *328*, 234.
(14) Brochard-Wyart, F. *C.R. Acad. Sci. Paris, Ser. 2* **1987**, *305* (8), 657.
(15) Bird, R. B.; Hassager, O.; Armstrong, R. C.; Curtiss, C. F. *Dynamics of Polymeric Liquids*, 2nd ed.; Wiley: New York, 1987; Vol. 2.
(16) Summerfield, G. C.; Ullman, R. *Macromolecules* **1987**, *20*, 401.
(17) Composto, R. J.; Kramer, E. J.; White, D. M. *Macromolecules* **1992**, *25*, 4167.
(18) Bachus, R.; Kimmich, R. *Polymer* **1983**, *24*, 964.
(19) Van Alsten, J. G.; Lustig, S. R. *Macromolecules* **1992**, *25*, 5069.
(20) Whitlow, S. J.; Wool, R. P. *Macromolecules* **1991**, *24*, 5926.
(21) Léger, L.; Hervet, H.; Rondelez, F. *Macromolecules* **1981**, *14*, 1732.
(22) Sanchez, I. C., Ed. *Physics of Polymer Surfaces and Interfaces*; Butterworth: Boston, 1992.
(23) Stockmayer, W. H. *Pure Appl. Chem.* **1967**, *15* (3), 247.
(24) Adachi, K.; Kotaka, T. *Macromolecules* **1984**, *17*, 120.
(25) Adachi, K.; Kotaka, T. *Macromolecules* **1985**, *18*, 466.
(26) Adachi, K.; Kotaka, T. *Macromolecules* **1988**, *21*, 157.
(27) Imanishi, Y.; Adachi, K.; Kotaka, T. *J. Chem. Phys.* **1988**, *89* (12), 7585.
(28) Boese, D.; Kremer, F. *Macromolecules* **1990**, *23*, 829.
(29) Riande, E.; Saiz, E. *Dipole Moments and Birefringence of Polymers*; Prentice-Hall: Englewood Cliffs, NJ, 1992.
(30) Fodor, J. S.; Hill, D. A. *Macromolecules* **1992**, *25*, 3511.
(31) Fodor, J. S.; Hill, D. A. *Macromolecules* **1993**, *26*, 5379.
(32) Fodor, J. S.; Hill, D. A. *J. Phys. Chem.* **1994**, *98*, 7674.
(33) Doi, M.; Edwards, S. F. *J. Chem. Soc., Faraday Trans. 2* **1978**, *74*, Parts 1–3, 1789.
(34) Adachi, K.; Itoh, S.; Nishi, I.; Kotaka, T. *Macromolecules* **1990**, *23*, 2554.
(35) Adachi, K.; Yoshida, H.; Fukui, F.; Kotaka, T. *Macromolecules* **1990**, *23*, 3138.
(36) Honerkamp, J.; Weese, J. *Continuum Mech. Thermodyn.* **1990**, *2*, 17.
(37) Honerkamp, J.; Weese, J. *Macromolecules* **1989**, *22*, 4372.
(38) Imanishi, Y.; Adachi, K.; Kotaka, T. *J. Chem. Phys.* **1988**, *89* (12), 7593.

(39) Lamb, H. *Hydrodynamics*; Cambridge University Press: Cambridge, U.K., 1932.
(40) Fodor, J. S.; Hill, D. A. *J. Rheol.* **1994**, *38* (4), 1071.
(41) Landau, L. D.; Lifshitz, E. M.; Pitaevskii, L. P. *Electrodynamics of Continuous Media, Course of Theoretical Physics*, 2nd ed.; Pergamon: New York, 1984; Vol. 8.
(42) Doi, M.; Onuki, A. *J. Phys. II* **1992**, *2* (8), 1631.
(43) Brochard-Wyart, F.; de Gennes, P.-G. *Makromol. Chem., Macromol. Symp.* **1990**, *40*, 167.
(44) Flory, P. J. *Principles of Polymer Chemistry*; Cornell University Press: Ithaca, NY, 1953.
(45) Ferry, J. D. *Viscoelastic Properties of Polymers*; John Wiley and Sons: New York, 1980.
(46) Graessley, W. W. *Adv. Polym. Sci.* **1982**, *47*, 67.
(47) Watanabe, H.; Tirrell, M. *Macromolecules* **1989**, *22*, 927.
(48) Larson, R. G. *Constitutive Equations for Polymer Melts and Solutions*; Butterworth: Stoneham, MA, 1988.
(49) Morton, M.; Fetters, L. J. *Anionic Polymerization: Principles and Practices*; Academic Press: New York, 1983.
(50) Morton, M.; Bostick, E. E.; Clarke, R. G. *J. Polym. Sci., Part A* **1963**, *1*, 475.
(51) Carslaw, H. S.; Jaeger, J. C. *Conduction of Heat in Solids*, 2nd ed.; Oxford University Press: New York, 1959.
(52) Ehlich, D.; Takenaka, M.; Hashimoto, T. *Macromolecules* **1993**, *26*, 492.
(53) Fleischer, G.; Fujara, F.; Stuhn, B. *Macromolecules* **1993**, *26*, 2340.
(54) Von Meerwall, E.; Grigsby, J.; Tomich, D.; Van Antwerp, R. *J. Polym. Sci., Polym. Phys. Ed.* **1982**, *20*, 1037.
(55) Cussler, E. L. *Diffusion Mass Transfer in Fluid Systems*; Cambridge University Press: Cambridge, U.K., 1984.

MA9412039